

# A Geiger-mode avalanche photodiode array for X-ray photon correlation spectroscopy

I. Johnson,<sup>a\*</sup> Z. Sadygov,<sup>b</sup> O. Bunk,<sup>a</sup> A. Menzel,<sup>a</sup> F. Pfeiffer<sup>a,c</sup> and D. Renker<sup>a</sup>

Received 1 September 2008

Accepted 21 October 2008

<sup>a</sup>Paul Scherrer Institut, 5232 Villigen PSI, Switzerland, <sup>b</sup>Joint Institute for Nuclear Research, 141980 Dubna, Russia, and <sup>c</sup>Ecole Polytechnique Fédérale de Lausanne, 1015 Lausanne, Switzerland.

E-mail: ian.johnson@psi.ch

X-ray photon correlation spectroscopy (XPCS) provides an opportunity to study the dynamics of systems by measuring the temporal fluctuations in a far-field diffraction pattern. A two-dimensional detector system has been developed to investigate fluctuations in the frequency range of several Hz to kHz. The X-ray detector system consists of a thin 100  $\mu\text{m}$  scintillation crystal coupled to a Geiger-mode avalanche photodiode array. In this article the elements of the system are detailed and the detector for XPCS measurements is demonstrated.

© 2009 International Union of Crystallography  
Printed in Singapore – all rights reserved**Keywords:** X-ray photon correlation spectroscopy; X-ray diffraction; photon correlation spectroscopy; dynamic light scattering; detector; Geiger-mode avalanche photodiode.

## 1. Introduction

Photon correlation spectroscopy (PCS), also known as dynamic light scattering, probes the dynamics of a target sample by analyzing the temporal correlations among scattered photons (Chu, 1991). Visible-wavelength PCS has proven to be a valuable technique for studying the long-wavelength hydrodynamics of fluids, including simple liquids, liquid mixtures, liquid crystals, polymers and colloidal suspensions. However, visible-wavelength PCS cannot probe the short-wavelength dynamics of materials or opaque samples. The X-ray analogue to PCS, X-ray photon correlation spectroscopy (XPCS), offers an unprecedented opportunity to extend the range of length scales over which a material's low-frequency dynamics can be probed down to interatomic distances (Chung *et al.*, 2006; Dierker *et al.*, 1995; Thurn-Albrecht *et al.*, 1996; Mochrie *et al.*, 1997; Price *et al.*, 1999).

Detector systems designed for XPCS must measure the intensity *versus* time in correlated regions, speckles, of the far-field diffraction pattern. As length scales of interest become smaller and move toward the nanoscale, measurements at higher momentum transfers need to be made. At higher momentum transfers, intensities are drastically reduced and fluctuations become faster. Thus detector systems should ideally combine high sensitivities with fast data sampling rates (Sikharulidze *et al.*, 2002).

We have developed a two-dimensional X-ray detector, shown in Fig. 1, to improve the sensitivity in probing weakly scattering systems, like rapidly fluctuating soft-matter systems. The detector system contains 64 independent channels. In principle, this increases the sensitivity by almost two orders of magnitude when compared with a typical point detector.

## 2. Detector

The X-ray-sensitive components are constructed from an array of Geiger-mode avalanche photodiodes (GMAPDs) (Sadygov *et al.*, 2003) optically coupled to a thin 100  $\mu\text{m}$  scintillation crystal array. A lutetium oxyorthosilicate (LSO) scintillation crystal is used to convert the X-ray's energy to visible light. The light output of LSO, 30 visible photons per keV of deposited energy, has a decay constant of about 40 ns. Thus the scintillation from a 6 keV X-ray releases about 90 visible photons in the first 50 ns. The crystal is pixelated into

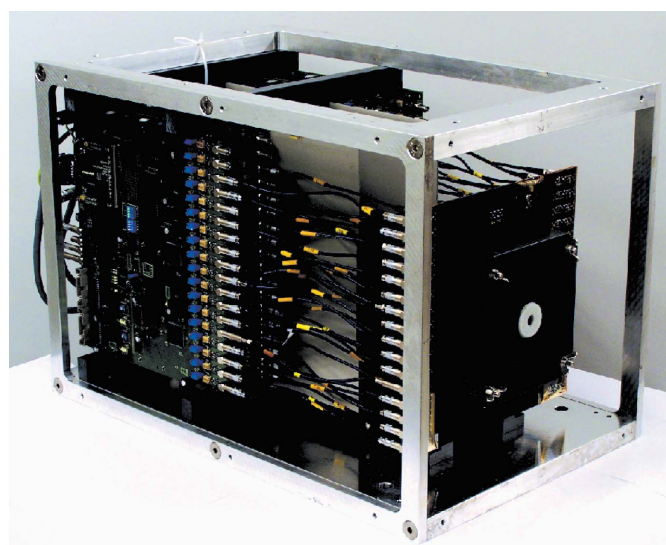


**Figure 1**  
Photograph of the detector.

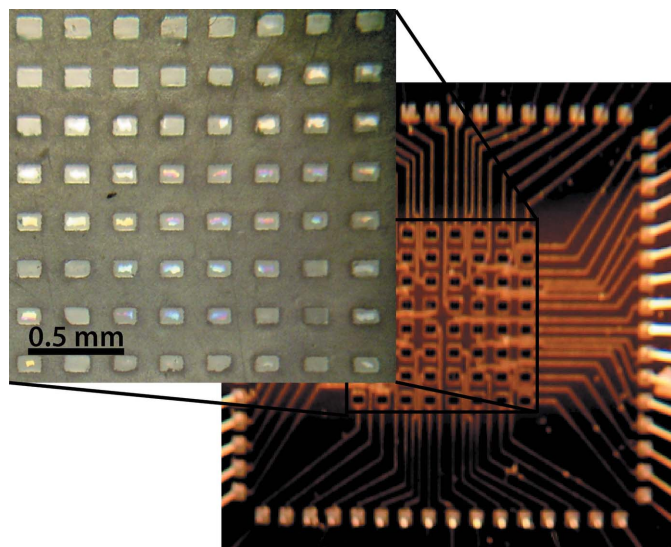


**Figure 2**  
Image of the LSO crystal array and the GMAPD array.

blocks that match the pitch of the GMAPD array, both shown in Fig. 2. Each crystal block is  $\sim 85 \times 125 \mu\text{m}$  and optically isolated from its neighbors to eliminate optical cross-talk. The diffuse reflective walls of the blocks channel the light to the GMAPD pixels. The single visible photon sensitivity of the GMAPD makes the combination sensitive down to an X-ray energy of a few keV. On the higher-energy side, the stopping power of the LSO allows for efficient detection up to tens of keV.

### 2.1. Geiger-mode avalanche photodiode array

Each detector pixel in the array consists of a  $100 \times 100 \mu\text{m}$  GMAPD. The cells are arranged in an  $8 \times 8$  array with a pitch of  $250 \mu\text{m}$ . Each cell can be thought of as a diode with a thin region of strong electric field at the p–n junction which is located a few micrometers below the surface. The diodes are operated above the breakdown voltage in the so-called Geiger mode. Each electron that travels across the high-electric-field region of the junction with high probability can initiate a self-sustaining avalanche of electrons that in turn generates a large number of carriers. Consequently, the current increase through the limiting resistor ( $R_b$  in Fig. 3) reduces the potential across the diode below the breakdown voltage, thus, passively quenching the breakdown within a nanosecond.

In an avalanche, about  $10^7$  electron–hole pairs are generated, leading to an easily measured signal. However, in this mode the diode completely breaks down, and as a result the number of charge carriers generated is independent of the initial number of electron–hole pairs. The initiation of a breakdown requires just one electron–hole pair to cross the junction region. This makes the diode sensitive to a single visible photon that frees one electron in the sensitive region above the junction. Similarly, thermally generated electron–hole pairs trigger breakdowns and lead to an unwanted dark count rate. At room temperature the average dark count rate per cell is about 52 kHz. This thermal generation of electron–

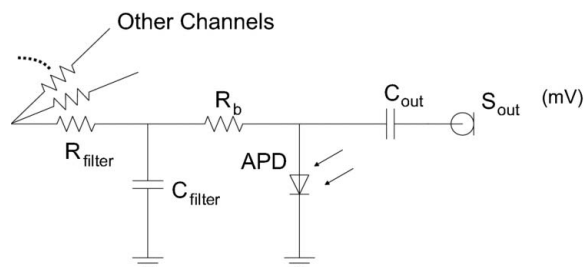


**Figure 3**  
Analog circuit of a single cell.

hole pairs and consequently the dark count rate decrease exponentially with temperature. The coefficient in the exponential is about 8 K for silicon. At the operation temperature, 214 K, this background count rate is reduced by more than three orders of magnitude to about 20 Hz.

The system is cooled by two stacked water-cooled Peltier elements. To avoid condensation on the cooled components an air-tight nitrogen-filled vessel encloses the system. Above the sensor, thin light-tight  $14 \mu\text{m}$  Pokalon polycarbonate films construct a triple-paned entrance window. This window construction avoids an abrupt temperature gradient and water condensation on the entrance window. The three layers attenuate the flux on the detector by 9.8% at 6 keV X-rays (or 3.5% at 8 keV).

Owing to the high flow of charges in a breakdown, many deep traps in the silicon are filled with electrons which are subsequently released with a time constant of several 100 ns, and can trigger a subsequent breakdown event. This results in another unwanted effect, the so-called afterpulsing. Since the number of filled deep traps depends on the total charge flowing in the diode, the decoupling capacitor ( $C_{out}$  in Fig. 3), which contributes to the current, has been chosen to be as small as possible (18 pF). Thus the number of afterpulses is reduced without decreasing the amplitude of the output signal by more than 20%. Choosing a capacitance near the lower limit also minimizes the bandwidth of electronic noise on the output signal.

A low-pass filter at the bias voltage input stabilizes the bias for channels individually and reduces electronic coupling. The value of the serial resistor,  $R_b = 6 \text{ k}\Omega$ , determines the recovery time of a pixel. After a breakdown, pixels are actively reset with current from the bias supply traveling through the serial resistor. This current exponentially recharges the bias across the diode and prepares the diode for the next breakdown. Given these values,  $\tau_{RC}$  of the recharge is about 100 ns. This is more than the time required to bring signals, after amplification with a MAR8 amplifier (Mini-Circuits; <http://www.mini-circuits.com/>), above the corresponding level of the threshold discriminator.

### 2.2. Readout

Digital pulses from the discriminated signals are directly fed into field-programmable gate arrays (FPGAs) on the front-end readout boards, as shown in Fig. 4. Four boards segment the readout into 16 channel blocks. Each board has three

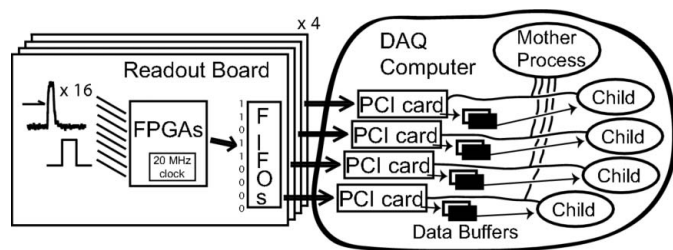


**Figure 4**  
Schematic of the readout architecture.

FPGAs that provide a digital processing freedom that can be optimized to fit the needs of a specific experiment. For XPCS, events are grouped into 50 ns frames. This sampling time was chosen to correspond to the 40 ns decay time of the LSO crystal. Frames that contain an event from at least one of the 18 channels on the board (16 of which are used by the APD array, two reserved for the integration with other detectors) are given a time stamp. The data are packed into a 32-bit word that consists of 18-bits for channel information and 14-bits for the time stamp, and transferred to two parallel 16-bit first-in–first-out (FIFO) data buffers. In order to keep track of the clock beyond its internal 819  $\mu\text{s}$  range, frames on clock roll-overs (16383 to 0) are always transferred to the FIFOs independent of whether an event occurred within the two cycles.

Data from the FIFOs are transmitted over a gigabit serial link, GigaSTaR (Inova Semiconductors; <http://www.inova-semiconductors.de/>) to a PCI card in the data acquisition (DAQ) computer. Each board has its own gigabit link and independently sends data to a PCI card. In this configuration the throughput of data is limited to the maximum bandwidth of the PCI bus, which is 133  $\text{MB s}^{-1}$ , *i.e.* 32 bits at 33.3 MHz. At the receiving end the PCI cards are set up for direct memory access, and 4 kB data packets are directly transferred to the data buffers in the system memory.

### 2.3. Data acquisition

The four PCI cards and processing/saving of data buffers are controlled by a mother DAQ process and four child processes (one for each PCI card), shown schematically in Fig. 4. When a data buffer is full, an interrupt signal from one of the PCI cards will wake up the mother process, initiate the switching of that data buffer (addresses only) and then the start of a new transfer. This dual buffer data swapping scheme for each PCI card allows simultaneous filling and reading of data and prevents reading/writing race conditions within data buffers. Once the data buffer pointers are swapped, the mother process communicates to the corresponding child process that its next data buffer is full and ready to be analyzed. Once the child has finished processing and writing the data to disk, it indicates to the system that it is finished with the ‘full buffer’ by enabling the interrupt signal in the PCI card driver. This completes the sequence and the system is prepared for the next cycle. The architecture, handled through interrupts, is one way of minimizing the CPU usage and traffic

on the PCI bus. Thus, the data transfer is optimized for both efficiency and speed.

Start and stop control signals are sent by UNIX commands over the gigabit links. The commands may be directly executed from the command line, through a DAQ graphical user interface, or *via* ssh. The start command launches the mother and children acquisition daemons, while the stop DAQ command sends end signals to these processes. Through a dedicated Certified Scientific Software’s (SPEC) library (<http://www.certif.com/>), these commands have been integrated into the global infrastructure of the coherent Small Angle X-ray Scattering beamline (cSAXS) of the Swiss Light Source, Paul Scherrer Institut, Switzerland. The library utilizes the remote execution feature *via* ssh keys. From SPEC, the DAQ can be started or stopped manually at the user interface or automatically in linear and two-dimensional scans.

Online, the child processes calculate the event rate of each channel and the average event rate. This information is stored in global memory that is periodically read by an online data display process. The online display is used for quality control and provides four plots: one- and two-dimensional graphs of the frequency *versus* pixel location, the frequency *versus* readout channel number and the historical frequency value of one chosen channel.

### 3. Intensity–intensity correlation function

Offline, the intensity–intensity correlation function,

$$g_2(\Delta t) = \frac{\langle I(t)I(t + \Delta t) \rangle}{\langle I(t) \rangle^2}, \quad (1)$$

is calculated for each channel. This function may be written in the following discrete form,

$$g_2(\Delta i) = \frac{N \sum I_i I_{i+\Delta i}}{(\sum I_i)^2}, \quad (2)$$

where  $I_i$  corresponds to the intensity in the  $i$ th time window and  $N$  is the total number of bins. In the software the time windows and, correspondingly, their spacing grow logarithmically. This logarithmic growth drastically reduces calculation time and memory usage. The software sequentially operates on the four 16 channel readout blocks and computes the 64 correlation functions.

### 4. Experimental results

We have conducted a demonstration experiment at the cSAXS beamline. The layout of the experiment is shown in Fig. 5. An X-ray energy of 6 keV ( $\lambda = 2 \text{ \AA}$ ) was chosen. The test sample, highly concentrated silica colloids ( $d = 110 \pm 3 \text{ nm}$ ) in an ethanol and benzyl alcohol solution, was illuminated with a  $25 \times 25 \mu\text{m}$  coherent (van der Veen & Pfeiffer, 2004; Pfeiffer *et al.*, 2005) portion of the monochromatic beam. The exit wave from the sample traveled 7.35 m through an evacuated flight tube to the detector. The center of the GMAPD array detector was positioned transversely off the beam axis by

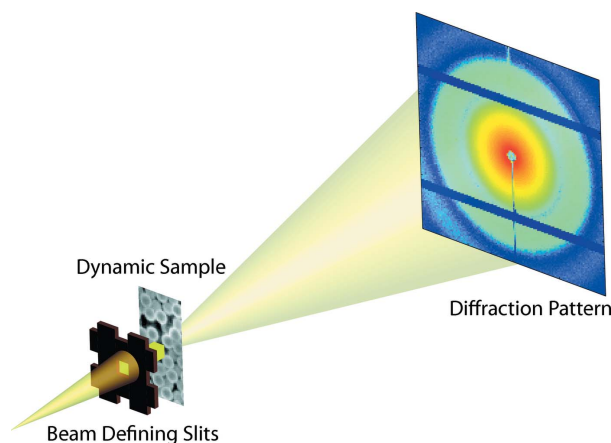


**Figure 5**  
Experimental set-up.

2.12 mm. The speckle size in this beamline geometry,  $\sim 60 \mu\text{m}$ , provided a good balance between flux into detector pixels and speckle contrast.

At the lowest momentum-transfer values,  $q = 0.004 \text{ nm}^{-1}$ , the flux into a pixel was about 1400 Hz, while the flux decreased to 300 Hz at  $q = 0.014 \text{ nm}^{-1}$ . At higher momentum transfers the lower flux into a pixel leads to a large statistical uncertainty in the correlation function at shorter lag-times,  $\Delta t$ , as can be seen in Fig. 6(a). On the other hand, the speckle contrast within each pixel resulted in a 4% visibility of the decay in the correlation functions, also shown in Fig. 6.

The correlation functions,  $g_2$  [equation (2)], can be related to the dynamics in the sample through the Siegert relation,

$$g_2(q, \Delta t) = 1 + \beta |g_1(q, \Delta t)|^2, \quad (3)$$

where  $\beta$  is the visibility of the correlation function and  $g_1$  is the normalized field correlation function.

#### 4.1. Results

In this demonstration the correlation functions for the 64 pixels have been fit with a purely exponential model,  $g_1(\Delta t) = \exp(-\Delta t/\tau)$ , with the characteristic relaxation time  $\tau$  as a free parameter. These relaxation times are plotted as a function of spatial frequency in Fig. 7. As the momentum transfer increases, the dynamics of the sample are probed on shorter length scales, leading to shorter relaxation times at higher momentum transfers.

This detector may be presently used to investigate the dynamics of samples in the range between a few milliseconds and several seconds. Although the readout architecture operates with a 20 MHz clock and samples events at this rate, present characteristics of the sensor limit the clean range of the data to time scales longer than a few milliseconds. Afterpulses that follow events introduce a strong positive correlation at short time scales. This positive correlation produces a background in the correlation function that extends into the hundreds of microsecond range with a percent level probability. Future developments could envision reaching sub-

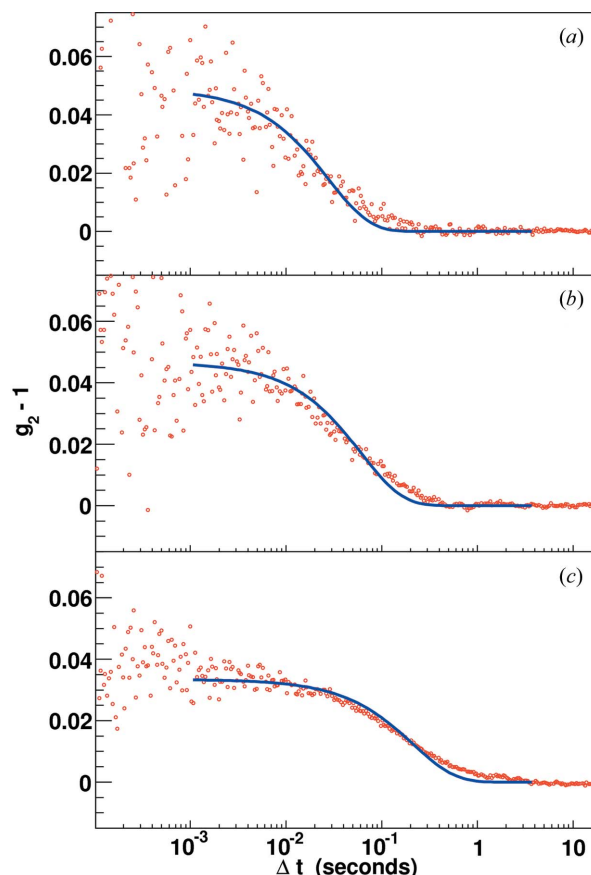


**Figure 6**  
Correlation functions for three pixels located at momentum transfers (a)  $q = 0.014 \text{ nm}^{-1}$ , (b)  $0.01 \text{ nm}^{-1}$  and (c)  $0.005 \text{ nm}^{-1}$ .

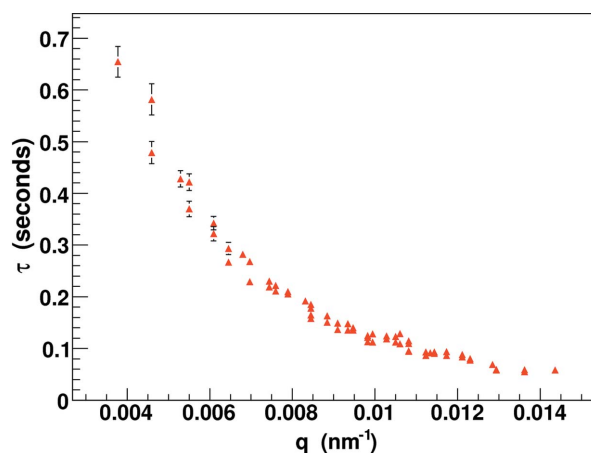


**Figure 7**  
Relaxation time ( $\tau$ ) versus momentum transfer ( $q$ ).

microsecond sampling times using this type of readout architecture in combination with a direct detection sensor.

#### 5. Conclusion

In summary, we have developed a two-dimensional detector system for X-ray photon correlation spectroscopy and demonstrated its performance. These results show that, with

a single data acquisition, multiple autocorrelation measurements at various momentum transfers may be simultaneously performed. This conceptual design inherently increases the sensitivity of such XPCS experiments when compared with the currently available fast 0D detector units. In addition, these simultaneous measurements intrinsically reduce the radiation damage on the sample when multiple momentum transfers are probed. Furthermore, this two-dimensional detection scheme allows for cross-correlation measurements between different pixels in the detector.

We are grateful for the technical help from P. Dick, R. Baldinger, Z. Hochman and T. Sakhelashvili. We also gratefully acknowledge the assistance of D. K. Satapathy during the experiments and H. Guo from Professor G. H. Wegdam's group at Van der Waals–Zeeman Instituut, Universiteit van Amsterdam, for preparing the colloidal sample. The experimental work has been performed at the Swiss Light Source, Paul Scherrer Institut, Villigen, Switzerland.

## References

- Chu, B. (1991). *Laser Light Scattering: Basic Principles and Practice*. San Diego: Academic Press.
- Chung, B., Ramakrishnan, S., Bandyopadhyay, R., Liang, D., Zukoski, C. F., Harden, J. L. & Leheny, R. L. (2006). *Phys. Rev. Lett.* **96**, 228301.
- Dierker, S. B., Pindak, R., Fleming, R. M., Robinson, I. K. & Berman, L. (1995). *Phys. Rev. Lett.* **75**, 449–452.
- Mochrie, S. G. J., Mayes, A. M., Sandy, A. R., Sutton, M., Brauer, S., Stephenson, G. B., Abernathy, D. L. & Grübel, G. (1997). *Phys. Rev. Lett.* **78**, 1275–1278.
- Pfeiffer, F., Bunk, O., Schulze-Briese, C., Diaz, A., Weitkamp, T., David, C., van der Veen, J. F., Vartanyants, I. & Robinson, I. K. (2005). *Phys. Rev. Lett.* **94**, 164801.
- Price, A. C., Sorensen, L. B., Kevan, S. D., Toner, J., Poniewierski, A. & Hołyst, R. (1999). *Phys. Rev. Lett.* **82**, 755–758.
- Sadygov, Z. Ya., Jejer, V. N., Musienko, Yu. V., Sereda, T. V., Stoikov, A. V. & Zheleznykh, I. M. (2003). *Nucl. Instrum. Methods Phys. Res. A*, **504**, 301–303.
- Sikharulidze, I., Dolbnya, I. P., Fera, A., Madsen, A., Ostrovskii, B. I. & de Jeu, W. H. (2002). *Phys. Rev. Lett.* **88**, 115503.
- Thurn-Albrecht, T., Steffen, W., Patkowski, A., Meier, G., Fischer, E. W., Grübel, G. & Abernathy, D. L. (1996). *Phys. Rev. Lett.* **77**, 5437–5440.
- Veen, F. van der & Pfeiffer, F. (2004). *J. Phys. Condens. Matter*, **16**, 5003–5030.